

Michael Candon<sup>1</sup>, Errol Hale<sup>1</sup>, Maciej Balajewicz<sup>2</sup>, Arturo Delgado-Gutiérrez<sup>1</sup>, Vincenzo Muscarello<sup>1</sup> & Pier Marzocca<sup>1</sup>

<sup>1</sup>Sir Lawrence Wackett Defence & Aerospace Centre, RMIT University, Melbourne, Victoria, Australia <sup>2</sup>Independent Researcher, Boulder, CO, USA

#### **Abstract**

Optimally sparse Taylor partial derivatives opens up exciting avenues for efficiently reducing the complexity of aeroelastic systems through nonlinear modelling. However, within this category of reduced order models (ROMs), the robustness observed in the linear regime often diminishes rapidly when faced with nonlinear dynamics, particularly variations in critical parameters such as dynamic pressure, control hinge linear stiffness, or freeplay. This paper addresses nonlinear sensitivity by employing an innovative approach: the interpolation of a library of nonlinear unsteady aerodynamic ROMs within a condensed parameter space defined by dynamic pressure and freeplay magnitude. The resulting ROM, based on Lagrange interpolation of sparse higher-order Taylor partial derivatives, demonstrates exceptional precision in simulating high-amplitude transonic limit cycle oscillations in an all-movable wing system with freeplay. It accurately captures the nonlinear instability region, encompassing up to 96% of the linear flutter boundary, across a range of freeplay values.

Keywords: Nonlinear Model Reduction, Unsteady Aerodynamics, Transonic Aeroelasticity, Freeplay, LCO

#### 1. Introduction

Odelling aeroelastic systems with discrete structural nonlinearities, such as freeplay, in the transonic flow regime presents several challenges, notably the coexistence of nonlinear aerodynamic loads with structural nonlinearity [1]. While linearising the nonlinear structural model is common practice in aeroelastic problems involving freeplay (using techniques like fictitious masses [2]), assuming aerodynamic linearization may be invalid for some transonic systems with minor parameter changes [3]. In such cases, to avoid the extensive computational burden of resolving forces at each time-step using computational fluid dynamics (CFD) codes, a wide array of nonlinear unsteady aerodynamic reduced order models (ROMs) can be utilised.

A comprehensive overview of the evolution of aeroelastic model reduction is provided in a recent article by Dowell [4]. In aeroelasticity, often only the nonlinear aerodynamic forces on the elastic structure need to be modelled, while details about the flow structure in the farfield can be disregarded. Hence, employing a functional series approach, typically a multi-variable Taylor series expansion (or Volterra series [5, 6, 7, 8, 9, 10]), where nonlinear aerodynamic forces on the structure are expressed as a function of the structural response, is a logical choice.

Non-parametric nonlinear model reduction methods, such as those based on polynomial functionals, may suffer from reduced generalizability. For complex nonlinear problems, this implies that convenient linear regime relations, like the linear relationship between generalised force and dynamic pressure, or insensitivity to linear/nonlinear control stiffness properties, may become obsolete.

This paper extends prior research by the authors [1], demonstrating that employing Lagrange interpolation of a library of linear and sparse nonlinear ROMs (containing Taylor partial derivatives), a compact sub-region of the space defined by dynamic pressure and freeplay can be accurately modelled. The ROM library is generated by optimising hyperparameters for aeroelastic performance at each discrete location of the subspace. The interpolation scheme then facilitates generating the ROM library with disparity in polynomial order, sparsity, sparsity pattern, and cardinality. In other words, as long as the ROM performance is satisfactory at the sampling locations, the shape and sparsity of the derivative tensors are inconsequential.

The interpolated aerodynamic ROM is applied to a three-dimensional aeroelastic stabilator model with freeplay undergoing high-amplitude Limit Cycle Oscillations (LCO).

### 2. Methodology

### 2.1 Multi-Variable Taylor Series Expansion of the Unsteady Aerodynamic Forces

Assuming that the unsteady aerodynamic forces on a structure can be described in discrete-time as a dynamic function of structural displacement by

$$Q\{n\} = f(u) \tag{1}$$

where the subscripts denotes the discrete time interval, Q represents a vector of generalised aerodynamic forces,  $u = \{u_n, u_{n-1}, u_{n-2}, \dots u_{n-k}\}^T$  is a vector that contains the history of generalised displacements, k defines the number of time lags and f() is an unknown nonlinear dynamic function. Then, provided that the system is mildly nonlinear and memory fading f(u) can be approximated using a multi-variable Taylor series expansion according to

$$f(u) \approx T(u)$$
 (2)

which is evaluated at a reference location  $oldsymbol{u}=oldsymbol{a},$  written in multi-index form as

$$T(\boldsymbol{u}) = f(\boldsymbol{a}) + \sum_{p_i=1}^{p} \frac{1}{p_i!} (\boldsymbol{u} - \boldsymbol{a})^{p_i} \boldsymbol{D}^{p_i}$$
(3)

where  $D^{p_i} = (\partial^{p_i} f)(a)$  is a tensor of partial derivatives of f(a) of order  $p_i$ . Specifically,  $D^1$  is the gradient of f(a),  $D^2$  is the Hessian matrix, and so on. Given that f(a) is not known a priori, the coefficients of  $D^{p_i}$  are estimated from input-output training data, *i.e.*, the coefficients are identified to minimise the error between the Taylor approximation and the true values by  $min||Q_n - T(u)||$ .

#### 2.2 Identification of the Taylor Partial Derivatives

The procedure for identifying the unsteady unsteady aerodynamic ROMs is now described. This definition is for a single-input single-output (SISO) system. The reader is referred to [8] for identification using a multi-input approach.

#### 2.2.1 Input and Output Matrices

Considering a total of m structural modes, the vector of outputs is constructed by exciting each  $j^{th}$  structural mode individually using the vector of inputs  $u_j \in \mathbb{R}^n$ , j = 1, ..., m and the resultant full-order

aerodynamic forces are projected onto each  $i^{th}$  structural mode to give:

$$Q^{ij} = \{Q_1^{ij}, Q_2^{ij}, \dots, Q_n^{ij}\}^T \in \mathbb{R}^n, i = 1, \dots, m, j = 1, \dots, m$$
(4)

where n is the total number of samples and  $Q^{ij}$  represents the generalised aerodynamic forces in mode i due to perturbation of mode j. To construct the matrix of inputs, first a lower left triangular circulant matrix is constructed from  $u_i$  (truncated for k time lags) to give:

$$\mathbf{L}^{j} = \begin{bmatrix} \mathbf{u}_{j}\{1\} & 0 & \dots & 0 \\ \mathbf{u}_{j}\{2\} & \mathbf{u}_{j}\{1\} & \dots & 0 \\ \vdots & \vdots & \ddots & 0 \\ \mathbf{u}_{j}\{n\} & \mathbf{u}_{j}\{n-1\} & \dots & \mathbf{u}_{j}\{n-k\} \end{bmatrix} \in \mathbb{R}^{n \times k}, j = 1, \dots, m \tag{5}$$

and the  $p^{th}$ -order polynomial expansion of the rows gives:

$$\mathcal{M}^{j} = \begin{bmatrix} \boldsymbol{u}_{j}\{1\} & 0 & \dots & 0 & \boldsymbol{u}_{j}\{1\}^{2} & 0 & \dots & 0 \\ \boldsymbol{u}_{j}\{2\} & \boldsymbol{u}_{j}\{1\} & \dots & 0 & \boldsymbol{u}_{j}\{2\}^{2} & \boldsymbol{u}_{j}\{2\}\boldsymbol{u}_{j}\{1\} & \dots & 0 \\ & & & \vdots & & \ddots & \\ \boldsymbol{u}_{j}\{n\} & \boldsymbol{u}_{j}\{n-1\} & \dots & \boldsymbol{u}_{j}\{n-k\} & \boldsymbol{u}_{j}\{n\}^{2} & \dots & & \boldsymbol{u}_{j}\{n\}^{p} \end{bmatrix} \in \mathbb{R}^{n \times \kappa}, j = 1, \dots, m$$
(6)

where  $\kappa = \sum_{l=1}^{p} {k+(l-1) \choose l}$ .

#### 2.2.2 Identification of the Reduced Order Model using Least-Squares

Identifying the coefficients of the partial derivatives is a linear problem [11], given for the system inputs and outputs by

$$Q^{ij} = \mathcal{M}^j d^{ij} \tag{7}$$

where  $d^{ij} = \{d_1^{ij}, d_2^{ij}, \dots, d_{\kappa}^{ij}\}^T \in \mathbb{R}^{\kappa}, i = 1, \dots, m, j = 1, \dots, m$  contains the flattened tensors of partial derivatives corresponding to the generalised aerodynamic forces for  $Q_i(u_j)$  which is an unknown. The full set of partial derivatives (no sparsity) can be identified by solving the inverse linear problem using pseudo-inverses:

$$d^{ij} = \mathcal{M}^{j+} Q^{ij} \tag{8}$$

where  $^+$  is the Moore-Penrose Pseudo-Inverse. Finally, iterating through each structural mode, all instances of  $d^{ij}$  are stored in a three-dimensional array  $\bar{D} \in \mathbb{R}^{m \times m \times \kappa}$ .

#### 2.2.3 Identification of the Reduced Order Model using Orthogonal Matching Pursuit

OMP is a greedy algorithm that recovers a sparse representation of a signal in a step-by-step iterative manner [12]. For an explicit definition of the OMP algorithm used in this work, the reader is referred to recent work by the authors [1]. The objective of OMP is to identify a sparse representation of d, denoted by  $d_s$ , by solving the NP-hard problem

$$\underset{d_s}{\operatorname{argmin}} ||d_s||_0$$
 subject to  $\mathscr{M} \boldsymbol{d_s} = \boldsymbol{Q}$  (9)

where  $||d_s||_0$  is the  $\ell_0$  pseudo-norm, or the number of non-zero elements in  $d_s$  which is referred to from now on as s. Eq. 9 can be solved directly using OMP, giving the **O**ptimal **S**parsity **ROM** (OS-ROM):

$$d_s^{ij} = OMP(\mathcal{M}^j, Q^{ij}) \tag{10}$$

Finally, iterating through each structural mode, all instances of  $d_s^{ij}$  are stored in a three-dimensional array  $\bar{D}_s \in \mathbb{R}^{m \times m \times \kappa}$ . Practically speaking,  $\bar{d}_s$  contains the optimal set of s-sparse coefficients of the  $p^{th}$ -order unsteady aerodynamic ROM, satisfying the linear problem in Eq. 7. This can be used in a time-marching aerodynamic or aeroelastic simulation to obtain the aerodynamic forces on the structure at each time interval.

### 2.3 Scheme for Direct Interpolation of the ROM Library

For an  $\mathcal{N}$ -dimensional parameter space, containing the parameters  $\chi_1, \chi_2, \ldots, \chi_{\mathcal{N}}$ , for  $N_R > 1$  sampled ROMs  $\bar{D}_T^i \in \mathbb{R}^{m \times m \times \kappa}, i = 1, \ldots, N_R$  that are constructed at operating points  $X_i = \{\chi_{1i}, \chi_{2i}, \ldots, \chi_{\mathcal{N}_i}\}$ , then the set of operating points of these ROMs  $\Lambda$  is given by

$$\Lambda = \{X_1, X_2, \dots X_{N_R}\}\tag{11}$$

Then the objective is to interpolate the basis of ROMs to construct a new ROM at the operating point  $X_{N_R+1} \notin X$ . Given that each sampled ROM  $\bar{D}_T^i$  can be generated with a different polynomial order and a different number of lag terms, disparity in the index locations of the terms in each ROM in the basis must be accounted for. Therefore a base vector  $d_{T_{10}}$  is created by identifying the ROM with the maximum number of terms for each derivative order separately, given by

$$d_{T_{l0}} = \{0, 0, \dots, 0\} \in \mathbb{R}^{\kappa_l} \tag{12}$$

where  $\kappa_I = \binom{k_{m1}}{1} + \binom{k_{m2}+1}{2} + \ldots + \binom{k_{mp}+(p-1)}{p}$ ,  $k_{mp}$  is the number of lag terms used to generate the largest  $p^{th}$ -order tensor in the basis, and therefore,  $d_{T_{l0}}$  contains the index of every coefficient in the basis. Lagrange polynomials are used to interpolate the ROM basis which, considering that each parameter can be defined by an interpolation scheme of different order  $p_{\mathcal{L}1}, p_{\mathcal{L}2}, \ldots, p_{\mathcal{L}N}$ , are given for the new operating conditions  $X_I$  by

$$ROM := \bar{D}_{T_I} = \sum_{R_1=1}^{p_{\mathcal{L}_1}+1} \sum_{R_2=1}^{p_{\mathcal{L}_2}+1} \dots \sum_{R_{\mathcal{L}}=1}^{p_{\mathcal{L}_N}+1} \mathcal{L}_{R_1,\dots,R_{\mathcal{N}}}(X_I) \bar{D}_{T}^{R_1,\dots,R_{\mathcal{N}}}$$
(13)

where

$$\mathscr{L}_{R_1,\dots,R_{\mathscr{N}}}(\boldsymbol{X}_I) = \prod_{\substack{0 \le k_1 \le p_{\mathscr{L}1} \\ k_1 \ne R_1}} \frac{\chi_{1I} - \chi_{1k_1}}{\chi_{1R_1} - \chi_{1k_1}} \dots \prod_{\substack{0 \le k_{\mathscr{N}} \le p_{\mathscr{L},\mathscr{N}} \\ k_{\mathscr{N}} \ne R_{\mathscr{N}}}} \frac{\chi_{\mathscr{N}I} - \chi_{\mathscr{N}k_{\mathscr{N}}}}{\chi_{\mathscr{N}R_{\mathscr{N}}} - \chi_{\mathscr{N}k_{\mathscr{N}}}}$$
(14)

where  $\chi_{\mathcal{N}k_{\mathcal{N}}}$  and  $\chi_{\mathcal{N}R_{\mathcal{N}}}$  are the operating conditions for parameter  $\mathcal{N}$  at sampling locations  $k_{\mathcal{N}}$  and  $R_{\mathcal{N}}$ , and  $\chi_{\mathcal{N}I}$  is the interpolated location of parameter  $\mathcal{N}$ .

#### 3. Nonlinear Aeroelastic Framework

#### 3.1 Modified AGARD 445.6 Wing

The AGARD 445.6 wing is a well known transonic benchmark case, with experiments conducted in the NASA transonic dynamic wind tunnel. The model consists of a tapered swept wing (see Figure 1(a)) with a NACA 65A004 airfoil section and sweep angle of 45 [°]. The material properties considered here are those of the weakened model (No. 3) [13]. For a comprehensive validation

of the AGARD benchmark model using aerodynamic impulse responses, see recent work by the authors [14], [15].

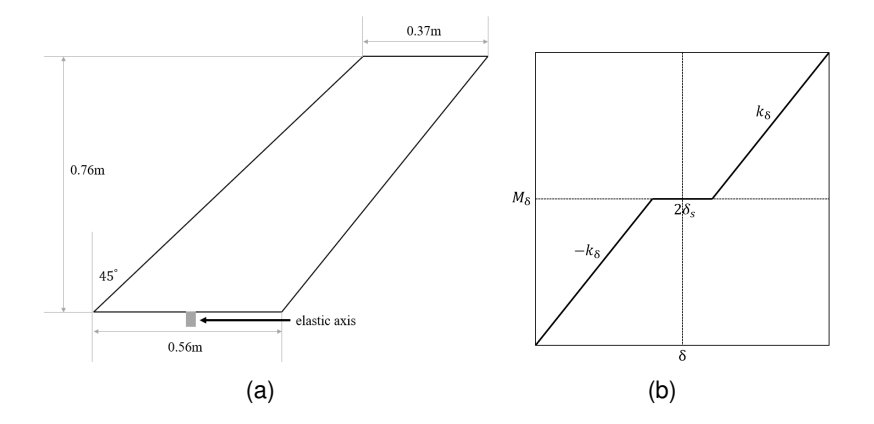


Figure 1 – a) Modified AGARD 445.6 wing geometry specifications and b) hinge stiffness as a function of rotation

In this paper, the wing is modified to represent an all-movable control surface (first presented by Carrese *et al.* [16]), with a torsional spring added to a centred node at the root, which is free to rotate about the pitch axis. The torsional spring contains a zero-stiffness dead-zone and a nominal stiffness of  $k_{\delta} = 500$  Nm/rad otherwise, as depicted in Fig. 1(b).

### 3.2 Nonlinear Aeroelastic Equations-of-Motion

The equation-of-motion for an aeroelastic system with concentrated structural nonlinearity in discrete (nodal) coordinates is given as

$$M_v \ddot{v} + R(\delta) + F_v = 0 \tag{15}$$

$$R(\delta) = K_v v + F_c(\delta) \tag{16}$$

where  $M_v$  and  $K_v$  are the structural mass and stiffness matrices,  $v = \{v_1, v_2, \dots, v_N\}^T$  is the displacement vector of N degrees-of-freedom, and  $\dot{v}$  is the time derivative of v.  $F_v = \{F_{v1}, F_{v2}, \dots, F_{vN}\}^T$  is the aerodynamic force vector in nodal coordinates. The freeplay loads are given by  $F_c(\delta)$  which is only non-zero at the node which contains freeplay, taking the form

$$F_{c}(\delta) = \begin{cases} k_{\delta}(\delta - \delta_{s}) & \delta > \delta_{s} \\ 0, & \text{if } -\delta_{s} < \delta < \delta_{s} \\ -k_{\delta}(\delta - \delta_{s}) & \delta < -\delta_{s} \end{cases}$$
(17)

where  $\delta$  is the rotational displacement of the root about the freeplay hinge axis and  $2\delta_s$  is the total rotational freeplay magnitude. The system described by Eq. (15) can be reduced by considering modal coordinates, such that the structural motion is approximated as the linear superposition of a subset of m normal modes  $\Phi_v$  due to generalised displacement  $\xi$ . Given the freeplay nonlinearity, the mode shapes in  $\Phi_v$  cannot properly account for localised displacements in the region of the nonlinear hinge. In this work, the fictitious masses (FM) method proposed by Karpel and Newman [2] is used to improve the representation of these local deformations in the set of low frequency modes. A large fictitious mass is added to the mode of the mass matrix where the discrepancy in localised displacements occurs, then the normal mode shapes are obtained from free vibration analysis and used in the aeroelastic simulation. The baseline FM modes  $\Phi_B$  are derived using ANSYS MAPDL, yielding the generalised system in baseline fictitious mass coordinates

$$M_B \ddot{\xi} + R_B(\delta) + Q = 0 \tag{18}$$

where  $M_B = \Phi_B^T M_v \Phi_B$ ,  $R_B(\delta) = \Phi_B^T K_v \Phi_B \xi + \Phi_B^T F_c(\delta)$ , and  $Q = \Phi_B^T F_v$  is the generalized aerodynamic force vector.

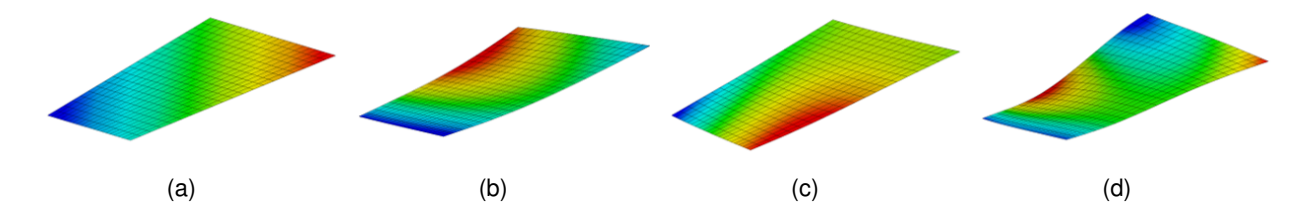


Figure 2 – First four fictitious mass modes with zero stiffness at the root with a) mode 1 (0Hz), b) mode 2 (28.24Hz), c) mode 3 (39.52Hz) and d) mode 4 (84.33Hz)

At this point it is important to note that in the general definition of the Taylor series expansion of the unsteady aerodynamic forces, the structural displacements defined by u (Eq. 1) are equivalent to  $\xi$  and will be referred to as such from now on.

### 3.3 Computational Fluid Dynamics Model

For the FOM, the generalised aerodynamic force vector Q is obtained using the commercial finite-volume Navier-Stokes solver ANSYS Fluent 2023 R1. The Euler equations for transient flowfields are solved via a coupled pressure-based solver with implicit second-order spatial and first-order temporal discretization of the flowfields with Rhie-Chow: distance-based flux interpolation. The convergence criteria are set to  $1\times 10^{-4}$  for the scaled residuals at each time-step. The investigation is conducted on a structured grid of  $70\times 10^3$  elements, with a minimum orthogonal quality of 0.032. It is important to note that this numerical mesh is validated against experimental campaign [13] via linear stability analysis [15, 16]. Grid deformation is facilitated using a diffusion-based approach. The Modal Projection and force Reconstruction (MPR) method [17] is used to project the structural mode shapes onto the fluid grid. MPR includes a robust interpolation scheme that accounts for disparity in the grid topologies, and conserves forces and moments.

## 3.4 Unsteady Aerodynamic ROM Library and Interpolation Scheme

#### 3.4.1 Generalised Aerodynamic Forces

Three separate sets of generalised aerodynamic forces are generated; using generalised displacements that are based on the natural frequencies and modal LCO amplitudes for i) the lowest dynamic pressure  $q_{\infty}=3768$  [Pa]  $(\bar{\xi}_A)$ , ii) the highest dynamic pressure of  $q_{\infty}=4012$  [Pa] with  $\delta_s=0.5^{\circ}$   $(\bar{\xi}_B)$ , and iii) the highest dynamic pressure with  $\delta_s=1^{\circ}$   $(\bar{\xi}_C)$ . Table 1 summaries the frequencies and maximum amplitudes of the random excitation of the generalised displacements for each mode. Four modes are used in the identification procedure which is the minimum number required for the basis to provide a good representation of the full-order structural model [18]. Figure 3 presents the total generalised aerodynamic forces in mode 2, comparing  $Q_{FOM}$ , the linear  $Q_{ROM}$  and the third-order  $Q_{OS-ROM}^{42}$ . The third-order ROM demonstrates a more than  $2\times$  reduction in error.

#### 3.4.2 Parametric Subspace

The parameter space is discretised according to nine separate sampled ROM locations  $\bar{D}_T^{ij}$  (Fig. 4). The ROMs are specifically targeted at freeplay values  $0.5^{\circ} \le \delta_s \le 1^{\circ}$ , and dynamic pressures  $3768[Pa] \le q_{\infty} \le 4102[Pa]$ , capturing the nonlinear instability region up to 96% of the flutter boundary.

Table 1 – Parameters of the band limited random excitation

|                   | Mode 1               |               | Mode 2 |               | Mod    | le 3          | Mode 4                  |               |  |
|-------------------|----------------------|---------------|--------|---------------|--------|---------------|-------------------------|---------------|--|
| ID                | f [Hz]               | $\xi_{1,max}$ | f [Hz] | $\xi_{2,max}$ | f [Hz] | $\xi_{3,max}$ | f [Hz]                  | $\xi_{4,max}$ |  |
| $\dot{ar{\xi}}_B$ | 0-35<br>0-35<br>0-35 | 0.03          | 0-35   | 0.02          |        | 0.02          | 0-100<br>0-100<br>0-100 | 0.01          |  |

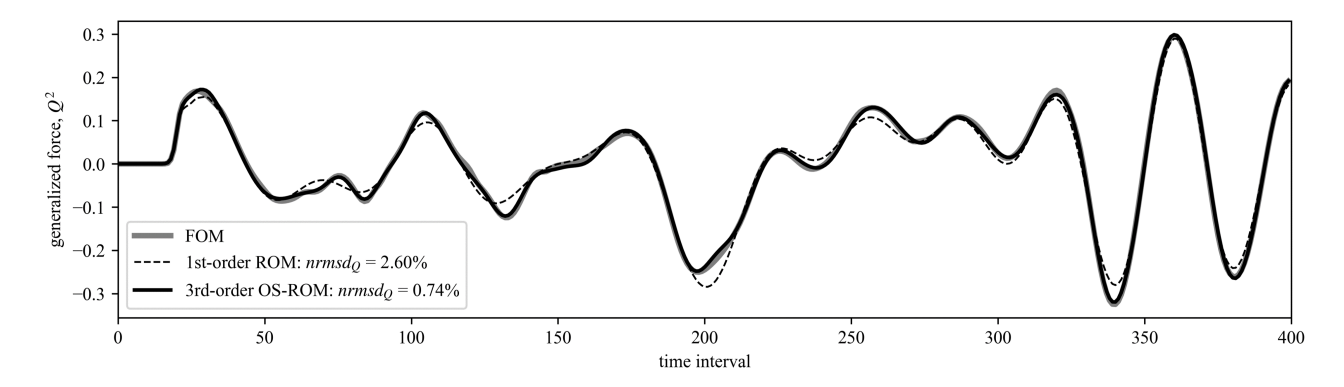


Figure 3 - Comparison between the FOM and ROM generalised aerodynamic forces for mode 2

#### 3.4.3 Hyperparameter Optimisation

Hyperparameter optimisation is conducted for each sampled ROM, *i.e.*, tuning the ROM to optimise aeroelastic performance at the discrete location of the subspace. For the lowest dynamic pressure linear models are generated using pseudo-inverses where  $\bar{\xi}_A$  is used to generate the generalised forces. For the highest dynamic pressure, OS-ROMs are generated using  $\bar{\xi}_B$  for  $\delta_s=0.5^\circ$  and,  $\bar{\xi}_C$  for  $\delta_s=0.75^\circ$  and  $\delta_s=1^\circ$ . To reduce the computational burden associated with ROM generation, the ROMs for the mid-point dynamic pressures are simply defined as some ratio between the ROM generated for the maximum and minimum dynamic pressures, according to

$$\bar{D_T}^{i2} = C_1 \bar{D_T}^{i1} + C_3 \bar{D_T}^{i3} \tag{19}$$

The aeroelastic optimisation problem uses the objective  $\operatorname{argmin}||\delta_{FOM}(t) - \delta_{ROM}(t)||$  which is quantified according to

$$nrmsd_{\delta} = nrmsd(\delta_{FOM}(t), \delta_{ROM}(t))$$
 (20)

where  $\delta$  is the rotational aeroelastic response at the root hinge node. The hyperparameters of the aeroelastic optimisation are summarised in Table 2.

Table 2 – Hyperparameter space for the aeroelastic optimisation

| ROM ID   | alg.                 | p | k        | S | $C_1$         | $C_3$ | objective  |
|--|----------------------|---|----------|---|---------------|-------|--|
| $egin{array}{c} ar{m{D}_{T}^{i1}} \ ar{m{D}_{T}^{i2}} \ ar{m{D}_{T}^{i3}} \end{array}$ | LS<br>interp.<br>OMP | 3 | <b>-</b> |   | -<br>0-1<br>- | 0-1   | $\operatorname{argmin}    nrmsd_{\delta}   $ $\operatorname{argmin}    nrmsd_{\delta}   $ $\operatorname{argmin}    nrmsd_{\delta}   $ |

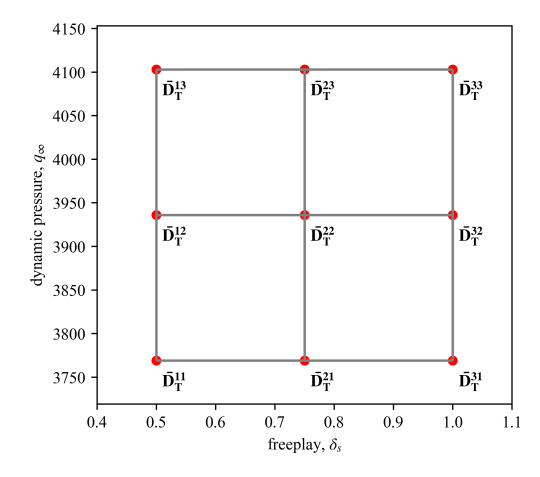


Figure 4 – Two-dimensional subspace and locations of the sampled ROMs

#### 3.4.4 Direct Interpolation Scheme

The discretization and interpolation schemes for the subspace are as follows; i)  $2 \times 2$  discretization of the subspace with bilinear interpolation (ROM<sub>4</sub><sup>1</sup>), and ii)  $3 \times 3$  discretization of the subspace with biquadratic interpolation(ROM<sub>9</sub><sup>2</sup>).

Given that both linear and third-order ROMs are used, and that the second-order and third-order partial derivatives are identified using the same number of lag terms, then the base vector (Eq. 23) is created using

$$\kappa_I = \binom{k_{m,lin}}{1} + \binom{k_{m,nl}+1}{2} + \binom{k_{m,nl}+2}{3} \tag{21}$$

The interpolated ROM is then derived for the new freeplay  $\delta_{s_I}$  and dynamic pressure  $q_{\omega_I}$  from Eq. 13, for interpolation scheme of order  $p_{\mathscr{L}}$  by

$$\operatorname{ROM}_{(p_{\mathscr{L}}+1)^2}^{p_{\mathscr{L}}} := \bar{\boldsymbol{D}}_{T_I} = \sum_{i=1}^{p_{\mathscr{L}}+1} \sum_{i=1}^{p_{\mathscr{L}}+1} \mathcal{L}_{ij}(\delta_{s_I}, q_{\infty_I}) \bar{\boldsymbol{D}}_T^{ij} \quad \text{where} \quad i \neq 2, j \neq 2 \quad \text{if} \quad p_{\mathscr{L}} < 2$$
 (22)

where

$$\mathscr{L}_{ij}(\delta_{s_I}, q_{\infty_I}) = \prod_{0 \le k_{\delta} \le p_{\mathscr{L}} \atop k_{\delta} \ne i} \frac{\delta_{sI} - \delta_{sk_{\delta}}}{\delta_{si} - \delta_{sk_{\delta}}} \prod_{0 \le k_q \le p_{\mathscr{L}} \atop k_q \ne j} \frac{q_{\infty_I} - q_{\infty k_q}}{q_{\infty_j} - q_{\infty k_q}}$$
(23)

### 3.5 Aeroelastic Time Integration

The aeroelastic system is solved using the RMIT in-house Fluid-Structure Interaction code PyFSI. Full-order aeroelastic solutions are achieved by marching Eq. 18 forward in time, where the wing transient structural motion is solved using Newmark- $\beta$  time-integration. Newton-Raphson iterations are used to converge the state-dependent freeplay load within each time-step by minimising error in the stiffness matrix. The nonlinear fluid loads Q are resolved at every time-step using the CFD model described above.

For nonlinear unsteady aerodynamic ROM solutions, substituting Eq, 7 into Eq. 18, the aeroelastic equation-of-motion becomes

$$M_B \ddot{\xi} + R_B(\delta) + q_\infty \mathcal{M}_B \bar{D}_{T_l} = 0 \tag{24}$$

where  $\mathcal{M}_B$  contains the aeroelastic response in FM coordinates, updated at every time-step by marching the system of equations forward in time using the approach described above. The linear

Table 3 – Hyperparameter optimisation results (\* are used in both ROM₄¹ and ROM₃²)

|   |         |              |                   |   | Hyperparameters |    |       |       |                      |
|---|---------|--------------|-------------------|---|-----------------|----|-------|-------|----------------------|
| ROM ID  | alg.    | $\delta_{s}$ | $q_{\infty}$ [Pa] | p | k               | S  | $C_1$ | $C_3$ | $nrmsd_{\delta}$ [%] |
| $ar{ar{D}_T^{11\star}}$                           | LS      | 0.5          | 3768              | 1 | 23              | -  | -     | -     | 0.71                 |
| $ar{ar{D}_{T}^{12}} \ ar{ar{D}_{T}^{13\star}}$    | interp. | 0.5          | 3923              | 3 | -               | -  | 0.43  | 0.57  | 0.78                 |
| $ar{m{D_T^{13}}}^\star$                           | OMP     | 0.5          | 4102              | 3 | 10              | 10 | -     | -     | 0.57                 |
| $ar{m{D}}_{m{T}}^{21}$                            | LS      | 0.75         | 3768              | 1 | 24              | -  | -     | -     | 0.96                 |
| $ar{m{D}_{T}^{22}}$                               | interp. | 0.75         | 3923              | 3 | -               | -  | 0.46  | 0.54  | 0.94                 |
| $ar{m{D}}_{m{T}}^{23}$                            | OMP     | 0.75         | 4102              | 3 | 15              | 13 | -     | -     | 1.71                 |
| $ar{ar{D}_{T}^{31}}^{\star} \ ar{ar{D}_{T}^{32}}$ | LS      | 1            | 3768              | 1 | 25              | -  | -     | -     | 1.77                 |
| $ar{m{D}}_{m{T}}^{ar{3}2}$                        | interp. | 1            | 3923              | 3 | -               | -  | 0.40  | 0.60  | 1.90                 |
| $ar{m{D}_{T}^{33\star}}$                          | OMP     | 1            | 4102              | 3 | 15              | 12 | -     | -     | 1.69                 |

scaling of the generalised aerodynamic forces with dynamic pressure is entirely valid for the interpolated ROM. A numerical time-step of  $\Delta t = 0.001$  s is used in all simulations.

#### 4. Results and Discussion

In this section the results of the aeroelastic ROM are presented and discussed. All simulations are conducted at  $M_{\infty}=0.96$  and  $\alpha_0=0^{\circ}$  with varying dynamic pressure and freeplay values.

#### 4.1 Sampled ROMs and Performance Without Interpolation

### 4.1.1 Aeroelastic Hyperparameter Optimisation

Table 3 summarises the results of the aeroelastic hyperparameter grid search. For the linear ROMs the optimal number of lag terms is relatively consistent, as to be expected. For the OS-ROMs, the optimal number of lag terms increases as the freeplay magnitude increases, *i.e.*, as the strength of the nonlinearity increases the memory fading nature of the system implies that more lags (or components in terms of Volterra kernels) are required. It is quite remarkable that high-precision ROMs can be identified with less than 15 total coefficients, where the full model is defined by hundreds. It should be noted that at  $\delta_s = 0.5$  [°],  $q_\infty = 3768$  [Pa], the system is actually marginally stable - captured by the FOM and ROM  $\bar{D}_T^{11}$ .

#### 4.1.2 Out-of-Sample Performance

To demonstrate the ROM out-of-sample performance without interpolation the linear ROM  $\bar{D}_T^{31}$  and third-order OS-ROM  $\bar{D}_T^{33}$  are considered and the dynamic pressure and freeplay magnitude are varied. Figure 5(a) presents the LCO amplitude at the hinge rotational axis as a function of dynamic pressure with a freeplay magnitude of  $\delta_s=1^\circ$ . It can be seen that, as expected, the third-order OS-ROM does not scale particularly well with dynamic pressure. That being said, considering the complexity and nonlinearity in the system, the result is reasonable and in line with the recent findings of Brown *et al.* [10] using a similar modelling approach. The linear ROM that has been tuned for aeroelastic performance at the lowest dynamic pressure of interest performs very poorly when scaled with dynamic pressure.

Figure 5(b) presents the LCO amplitude as a function of freeplay magnitude, dynamic pressure remains constant at the exact values that the linear ROM  $\bar{D}_T^{31}$  and third-order OS-ROM  $\bar{D}_T^{33}$  were calibrated to. The third-order OS-ROM generalises quite well, aside from an over prediction of the amplitude of the LCO for the lowest freeplay value of  $\delta_s = 0.5^\circ$ . The linear ROM also performs very

well, however, is unable to capture the stable response at  $\delta_s = 0.5^{\circ}$ . Despite generally good performance in terms of new freeplay values, the over prediction at the lowest freeplay value means that in order to derive a nonlinear ROM that is highly accurate across the entire parameter space, interpolation is necessary.

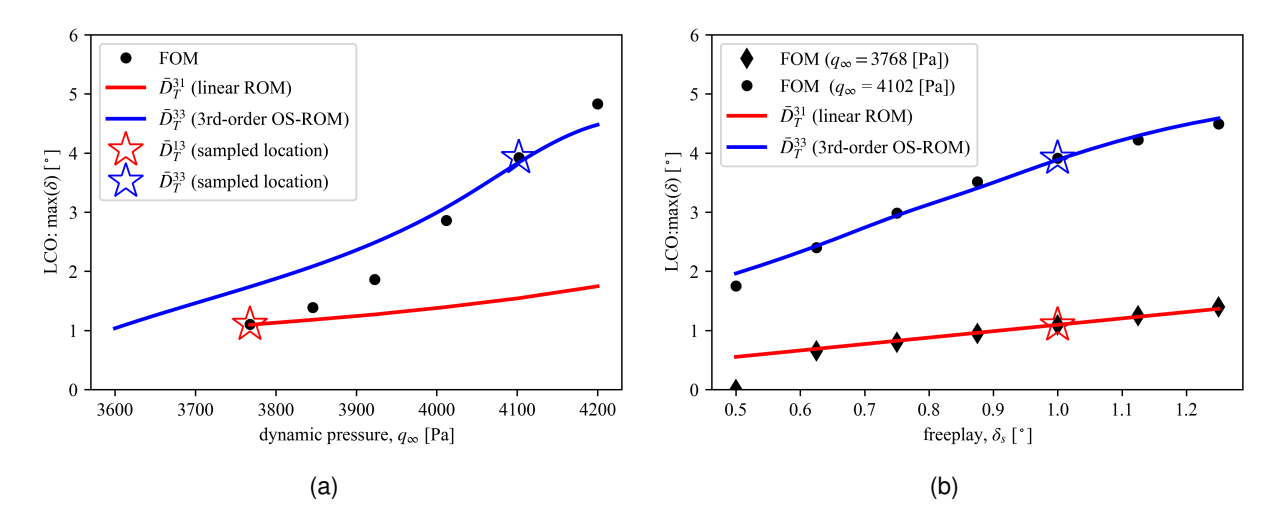


Figure 5 – LCO amplitude at the hinge rotational axis without interpolation

### 4.2 Interpolated ROM Performance

#### 4.2.1 Limit Cycle Amplitude

The out-of-sample performance of the two interpolated ROMs is first investigated in terms of the ability to capture the transonic limit cycle amplitudes.

Figure 6 presents the LCO amplitude predictions for the entire parameter space. As mentioned previously, at the lowest dynamic pressure and freeplay the system is found to be stable and the sampled ROM is tuned to capture this. Although this was not by design, it is an excellent finding that the inclusion of this ROM in the library allows robust identification of the nonlinear flutter point. Figure 6(a) demonstrates that at  $\delta_s = 0.5^\circ$  the bilinear ROM $_4^1$  captures the LCO amplitudes at the root rotational axis with very good precision and reasonable precision for  $\delta_s = 0.625^\circ$ . However, for freeplay values above this, discrepancies can be observed through under prediction of the LCO amplitude as the dynamic pressure increases beyond  $q_\infty = 3846$  [Pa]. Figure 6(b) presents the LCO amplitudes modelled using the biquadratic ROM $_9^2$ . Excellent agreement can be observed between the FOM and ROM solutions - demonstrating that the nonlinear parameter space can indeed be captured with excellent precision using a biquadratic interpolation scheme. Although not presented here, almost identical trends are observed for the tip response using ROM $_4^1$  and ROM $_9^2$ .

### 4.2.2 Limit Cycles in Generalised Coordinates

To probe the ROM performance further, the generalised displacements are now investigated comparing the FOM to the biquadratic ROM $_9^2$  solutions. Figure 7 presents bifurcation diagrams for each mode with freeplay  $\delta_s = 0.875^\circ$ , *i.e.*, plotting the maxima and minima of the generalised displacements at the five dynamic pressure validation locations. It can be seen that mode 1 is captured with excellent precision. Modes 2 and 3 are also captured well, however, some asymmetry can be observed at the highest dynamic pressure in the ROM which leads to a slight over prediction and there is a general under prediction at the lowest dynamic pressure. The dynamics of mode 4 present more interesting quasi-periodic behavior. It is quite impressive that the biquadratic ROM $_9^2$  is able to capture these dynamics quite well, including bifurcations that appear to occur between  $q_\infty = 3846$  [Pa] and  $q_\infty = 4012$ 

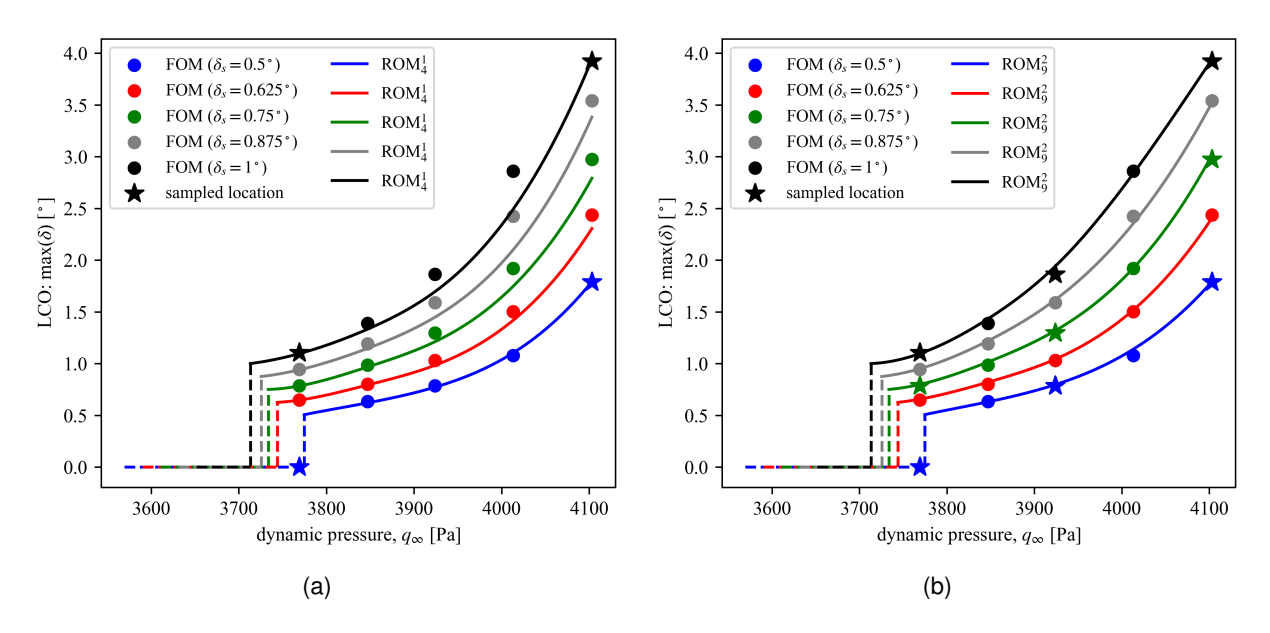


Figure 6 – LCO amplitude as a function of dynamic pressure at the root rotational axis comparing a) FOM to  $ROM_0^1$  and b) FOM to  $ROM_0^2$ 

[Pa], *i.e.*, the transition from a five period to three-period response. The lowest dynamic pressures present more error for mode 4, which is likely due to the low amplitude at this speed making it difficult to resolve. These discrepancies to not impact the global response in nodal coordinates.

Phase portraits of the generalised displacements are presented in Fig. 8 for the dynamic pressure  $q_{\infty}=4012$  [Pa]. For the lower freeplay  $\delta_s=0.625^{\circ}$  the biquadratic ROM $_9^2$  performance is very good for all modes. For the larger freeplay  $\delta_s=0.875^{\circ}$  mode 1 is captured with excellent precision while mode 2 and mode 3 demonstrate small discrepancies - not surprising given that this is at the centroid the most nonlinear quadrant of the parameter space. For mode 4 the five-period response is captured, however, asymmetry and associated discrepancies in amplitude can be observed. The accuracy of the ROM could be potentially be improved using a multi-input identification framework, or certainly by optimising the ROM in generalised coordinates, rather than for a single location in nodal coordinates.

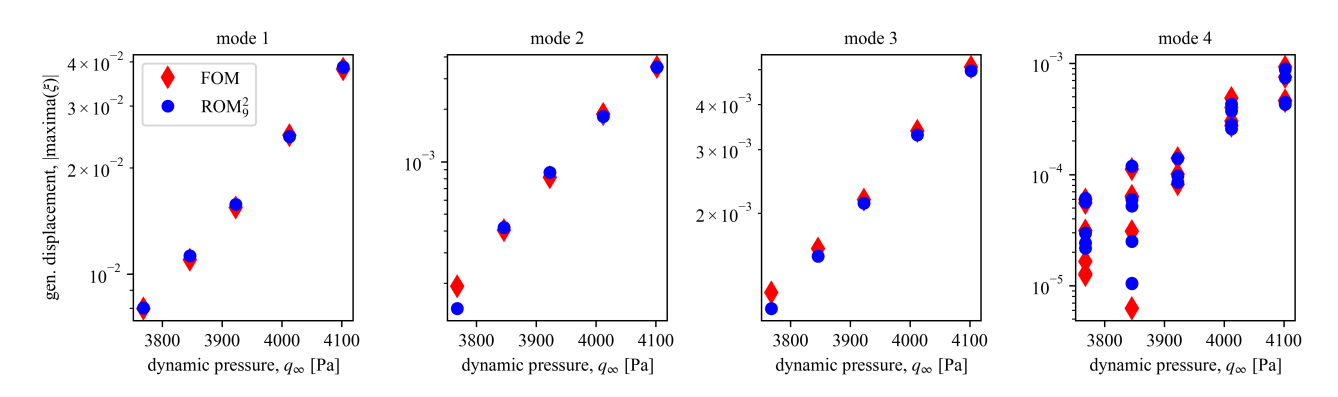


Figure 7 – Bifurcation diagrams in generalised coordinates comparing FOM to ROM<sub>9</sub><sup>2</sup> solutions displaying the maxima of the LCO (logarithmic scale)

### 4.3 Computational Savings

To ensure a stable limit cycle is achieved, 3000 numerical time-steps are required. Any CFD-based aerodynamic solutions are run on an Intel Xeon Gold 6152 CPU using 16 cores, while any ROM

11

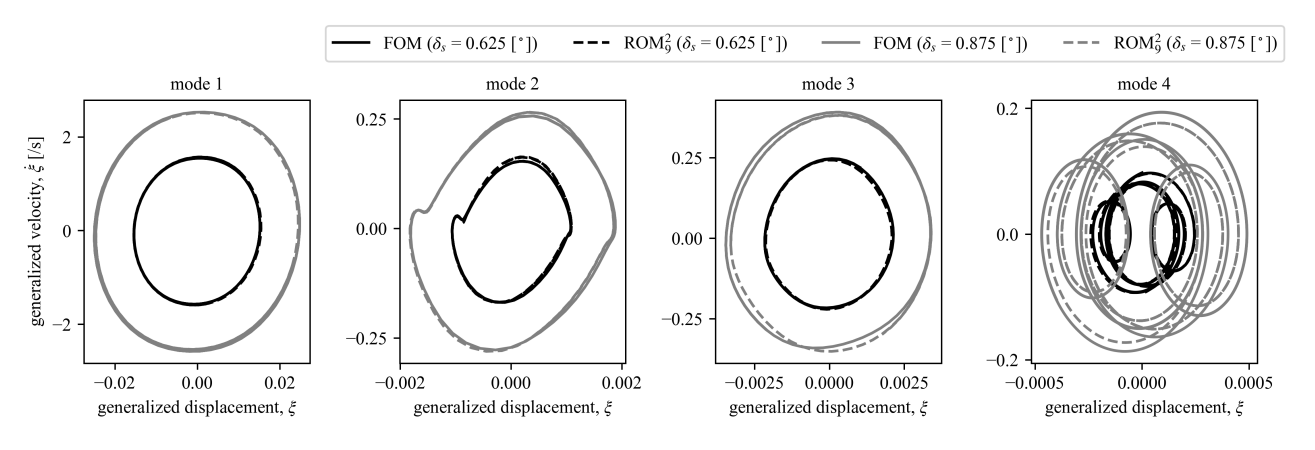


Figure 8 – Limit cycles in generalised coordinates at  $q_{\infty}$  = 4012 [Pa] comparing the FOM to ROM<sub>9</sub> solutions

solutions on a single core, *i.e.*, the resources are insignificant. In terms of simulation time, the ROM solutions are three orders of magnitude faster. However, the time taken to generate the ROM must also be taken into account. The ROM $_4^1$  takes approximately 22 hours to generate, while the ROM $_9^2$  takes approximately 40 hours to generate.

### 5. Summary and Conclusion

In this paper an approach for parameterising nonlinear non-parametric unsteady aerodynamic ROMs is presented. The application is to complex nonlinear aeroelastic systems. The approach considers direct interpolation (using Lagrange polynomials) of an aeroelastic-tuned unsteady aerodynamic ROM library. The library contains a combination of linear and optimally sparse nonlinear tensors of Taylor partial derivatives, equivalent to Volterra kernels.

The example given considers a 3D aeroelastic stabilator model with freeplay undergoing high amplitude LCO. The nonlinear unsteady aerodynamic ROM is parameterised in dynamic pressure and freeplay magnitude. A bilinear interpolation of the subspace performs very well for low freeplay values and dynamic pressures, while to model the entire subspace with high accuracy a biquadratic scheme is necessary.

The online computational savings are more than three orders of magnitude. The time taken to generate the ROM is also of significance. It is estimated that it takes 8-16 times longer to generate the nonlinear ROM library, than generating the linearized aerodynamic impulse responses for this same system.

In conclusion, this work demonstrates that it is possible to generate a highly accurate nonlinear unsteady aerodynamic ROM that is as robust to parameter changes as a linearized ROM within the linear regime, albeit with a larger but reasonable offline computational cost. Generating the same ROM without sparsity promotion would be computationally prohibitive.

#### 6. Acknowledgements

Thank you to the Australian Defence Science and Technology Group (DSTG) for their support in this collaborative research with RMIT University.

#### 7. Contact Author Email Address

mailto: candon.michael@rmit.edu.au

#### 8. Copyright Statement

The authors confirm that they, and/or their company or organisation, hold copyright on all of the original material included in this paper. The authors also confirm that they have obtained permission, from the copyright holder of any third party material included in this paper, to publish it as part of their paper. The authors confirm that they give permission, or have obtained permission from the copyright holder of this paper, for the publication and distribution of this paper as part of the ICAS proceedings or as individual off-prints from the proceedings.

#### References

- [1] M. Candon, E. Hale, M. Balajewicz, A. Delgado-Gutierez, and P. Marzocca. Optimal sparsity in nonlinear reduced order models applied to an all-movable wing with freeplay in transonic flow. *65<sup>th</sup> Structures, Structural Dynamics, and Materials Conference*, Orlando, FL 2024.
- [2] M. Karpel and M. Newman. Accelerated convergence for vibration modes using the substructure coupling method and fictitious coupling masses. *Israel Journal of Technology*, 13(1):55–62, May 1975.
- [3] M. Candon, R. Carrese, H. Ogawa, P. Marzocca, C. Mouser, O. Levinski, and W. Silva. Characterization of a 3dof aeroelastic system with freeplay and aerodynamic nonlinearities part i: Higher–order spectra. *Mechanical Systems and Signal Processing*, 118:781–807, 2019.
- [4] E. Dowell. Reduced-order modeling: A personal journey. Nonlinear Dynamics, 11:9699–9720, 2023.
- [5] W. A. Silva. *Discrete-Time Linear and Nonlinear Aerodynamic Impulse Responses for Efficient CFD Analyses*. PhD thesis, Ph.D. Thesis, College of William & Mary, Williamsburg, VA, December 1997.
- [6] Daniella E. Raveh. Reduced-order models for nonlinear unsteady aerodynamics. *AIAA Journal*, 39(8):1417–1429, 2001.
- [7] P. Marzocca, L. Librescu, and W. A. Silva. Time-delay effects on linear/nonlinear feedback control of simple aeroelastic systems. *Journal of Guidance, Control, and Dynamics*, 28(1):53–62, 2005.
- [8] M. Balajewicz and E. H. Dowell. Reduced-order modeling of flutter and limit-cycle oscillations using the sparse volterra series. *Journal of Aircraft*, 49(6):1803–1802, 2012.
- [9] N. de Paula and F. Marquez. Multi-variable volterra kernels identification using time-delay neural networks: Application to unsteady aerodynamic loading. *Nonlinear Dynamics*, 97:767–780, 2019.
- [10] C. Brown, G. McGowan, K. Cooley, J Deese, T. Josey, E. H. Dowell, and J. P. Thomas. Convolution/volterra reduced-order modeling for nonlinear aeroelastic limit cycle oscillation analysis and control. AIAA Journal, 60(12):6647–6664, 2022.
- [11] W. J. Rugh. Nonlinear System Theory. The Volterra/Wiener Approach. University Press, Baltimore, 1981.
- [12] S. Foucart and H. Rauhut. *A Mathematical Introduction to Compressive Sensing*. Birkhäuser, New York, 2013.
- [13] E. C. Yates. Agard-r-765 agard standard aeroelastic configurations for dynamic response i-wing 445.6. 61st Meeting of the Structures and Materials Panel, Oberammergau, Germany, September 1985.
- [14] E. Hale, V. Muscarello, P. Marzocca, and O. Levinski. Generation of generalised aerodynamics forces through cfd-based methods for aeroelastic stability analysis. *64<sup>th</sup> AIAA/ASCE/AHS/ASC Structures, Structural Dynamics, and Materials Conference*, National Harbour, Maryland, 2023.
- [15] M. J. Candon. Physical Insights, Characteristics and Diagnosis of Structural Freeplay Nonlinearity in Transonic Aeroelastic Systems: A System Identification Based Approach. PhD thesis, Royal Melbourne Institute of Technology, Melbourne, AU, December 2019.
- [16] R. Carrese, N. Joseph, P. Marzocca, and O. Levinski. Aeroelastic response of the agard 445.6 wing with freeplay nonlinearity. 58<sup>th</sup> AIAA/ASCE/AHS/ASC Structures, Structural Dynamics, and Materials Conference, Grapevine, Texas, 2017.
- [17] N. Joseph, R. Carrese, and P. Marzocca. Projection framework for interfacial treatment for computational fluid dynamics/computational structural dynamics simulations. *AIAA Journal*, 59(6):2070–2083, 2021.
- [18] E. Hale, M. Candon, V. Muscarello, and P. Marzocca. Evaluation of generalised forces using cfd-based methods for efficient linear/nonlinear simulations. 65<sup>th</sup> Structures, Structural Dynamics, and Materials Conference, Orlando, FL 2024.